ACS OMEGA

Open Access

This article is licensed under CC-BY-NC-ND 4.0

http://pubs.acs.org/journal/acsodf

Article

High-Performing and Stable Membrane Electrode Assemblies Based on Fluorine-Doped Tin Oxide Catalysts

Sofia Delgado, Vincent Wilke, Rita Marques, Jonathan Ruiz Esquius, Aldo Gago, Fátima Santos, Andreas Friedrich,* and Adélio Mendes*

Cite This: *ACS Omega* 2026, 11, 69026−69037

Read Online

ACCESS | Metrics & More | Article Recommendations | Supporting Information

ABSTRACT: To improve the iridium utilization on proton exchange membrane water electrolysers (PEMWEs), a new support based on fluorine-doped tin oxide (FTO) nanoparticles was developed, characterized, and assessed for the anode side. This approach utilizes a sol−gel method combined with a 500 °C annealing treatment to promote favorable metal−support interactions and contribute to catalyst stability. The resulting IrO_x/FTO catalyst exhibits remarkable performance at a low Ir loading of 0.5 mgIr cm^{-2}, corresponding to half the loading of the commercial IrO_2 reference. The membrane electrode assembly (MEA) incorporating the FTO-based anode outperformed the electrolyzer employing commercial IrO_2, reaching 1.35 A cm^{-2} at 2 V and 60 °C compared with 0.9 A cm^{-2} for the commercial catalyst. Moreover, these catalysts demonstrated excellent operational stability, with no significant activity decline during more than 300 h of continuous operation at 1.3 A cm^{-2} and 80 °C. These findings pave the way for innovative and cost-effective membrane electrode assemblies with enhanced stability.

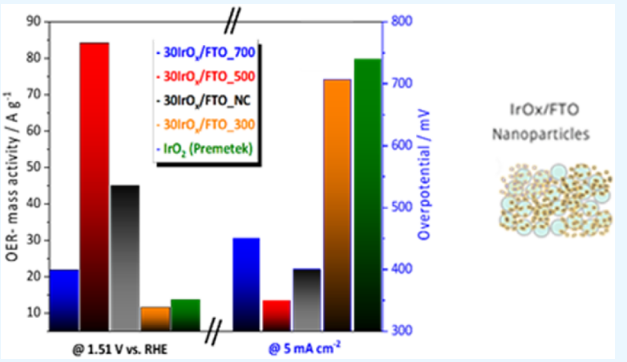

1. INTRODUCTION

The European Commission relies largely on the cheap production of green hydrogen for swift energy decarbonization. Proton exchange membrane water electrolyzers (PEMWE) are a promising technology for this transition, offering advantages such as high electrical efficiency, small carbon footprint, and excellent hydrogen gas purity after gas−liquid separation.[1] Additionally, PEMWEs can operate at high current densities and under rapidly varying power input, making them well suited for integrating with intermittent renewable energy sources. Despite their attractive features, PEMWEs encounter substantial obstacles that must be overcome to expedite their commercialization and fulfill the ambitious objectives of the European Commission of yielding 500 GWh of hydrogen by 2050. The major barrier to reaching this objective is the scarcity of the required noble metals for preparing the catalysts, which also account for ca. 10% of the total stack cost. For the hydrogen evolution reaction (HER) platinum (Pt)-based catalysts are normally employed, while for the oxygen evolution reaction (OER) iridium (Ir)-based catalysts are required. At a typical Ir loading of 1−2 mg_{Ir} cm^{-2} and a power density of 4 W cm^{-2}, approximately 250−500 kg of Ir are needed *per* gigawatt of installed capacity, which is a significant and insurmountable hurdle due to iridium's limited global production of only 9 tonnes per year.[2,3] Both the US Department of Energy (DOE)[4] and the European FCH-JU state that for PEMWE to be competitive in such large-scale applications, investment costs must be reduced by at least two-thirds, reaching a target of 300−600 euros per kilowatt.

As a result, several strategies have been proposed to minimize the loading of noble catalysts, in particular Ir, and maximize their utilization during OER, to achieve an energy density target of ca. 0.01 g_{Ir} kW^{-1} at 1.79 V (assuming loadings of *ca.* 0.05 mg_{Ir} cm^{-2}).[5] The strategies include (i) the particle size reduction to ensure higher surface-to-mass ratios by supporting precious metals onto conductive supports or (ii) the production of tunable 3D microstructures, e.g., highly active skeletons via selective leaching, with a very large specific surface area; (iii) the production of core−shell structures, where the core is made of a nonplatinum group metal (PGM) and the shell is a PGM catalyst[6,7] and other (iv) alloy-based structures with modified binding energies to increase stability and decreasing the need of PGA metals.[8,9] A significant challenge associated with reducing the amount of PGM use for the OER and the HER lies in keeping or increasing their long-term stability. This requirement is particularly challenging for the OER due to the harsh local acidic environment and

Received: July 29, 2026
Revised: September 14, 2026
Accepted: September 17, 2026
Published: October 29, 2026



ACS Publications

© 2026 The Authors. Published by American Chemical Society

Downloaded from pubs.acs.org/acsodf/article-pdf/11/44/69026/6903792/acsomega.6c08923.pdf by UNIVERSIDADE DO PORTO 01100 user on 25 November 2026

prevailing high oxidizing potentials, which trigger a series of detrimental degradation mechanisms, including catalyst delamination, membrane thinning, Ir dissolution, and agglomeration.[10,11] To avoid the formation of an insulating oxide layer during OER, conductive oxides were employed, such as SnO_2 doped with In-, Ta-, Nb-, Nb-, and Sb-.[12,13] In particular, SnO_2:Sb—antimony-doped tin oxide (ATO)—has been reported by Li Wang et al., to drop the loading of precious metal by 70%, while overcoming the high electrical resistivity of the anodic catalyst layers.[14] Even though some groups report excellent stabilities, there is no agreement on the applicability of Ir/SnO_2:Sb catalysts for OER, as some reports show high dissolution rates for both Ir and Sb.[14,15] Depending on the synthesis route and operating conditions, the dopant itself is prone to corrode.[16] On the other hand, after analyzing the time-dependent dissolution of dopants In, F, and Sb from tin oxide-based nanoparticles or films, fluorine-doped tin oxide (SnO_2:F, FTO) films were assigned promising supports for OER electrocatalysts in both acidic and alkaline media, due to its unmatched electrochemical stability window from −0.34 $V_{RHE} < E < 2.7$ V_{RHE}, surpassing that of both ATO and Ir/In-SnO_2 (ITO) nanoparticles.[16] Unlike ATO or ITO, the FTO doping procedure includes replacing the oxygen atoms with fluorine, an anion, rather than cation exchange, resulting in kinetically stable oxides.[17] Although FTO films offer remarkable stability, their limited surface area and inferior electrical conductivity hinder their application in large-scale anodes.[16] To overcome these limitations, focused attention is required to develop FTO nanoparticles/nanoplatelets with significantly enhanced surface area and electrical conductivity. Given these considerations, current research focuses on designing appropriate metal oxide supports that interact more effectively with catalysts to optimize the charge transfer pathways. To address the challenges associated with developing high-performance OER catalysts, this work focuses on preparing highly conductive fluorine-doped tin oxide supports using a sol−gel precursor. The FTO substrates are then modified with small and highly dispersed Ir nanoparticles via a modified polyol method. This approach yields high OER activity and stability, outperforming a commercial IrO_2-based catalyst with a significantly lower Ir loading.

The prepared MEAs using FTO-based anodes outperform an electrolyzer utilizing a commercially available IrO_2 catalyst, reaching 1.35 A cm^{-2} at 2 V and 60 °C compared with 0.9 A cm^{-2} for the commercial catalyst. The stability of these catalysts is remarkable, demonstrating no activity decline over 300 h of operation at 80 °C under high-current-density conditions. The findings pave the way for innovative and cost-effective membrane electrode assemblies with enhanced stability.

2. EXPERIMENTAL SECTION

2.1. Synthesis of Electrocatalysts

FTO nanoparticles were prepared using a modified sol−gel method. 80 mL of absolute ethanol was added to 10.52 g of $SnCl_4 \bullet 5H_2O$ and stirred for 2 h. Simultaneously, 20 mL of distilled water was added to 1.67 g of NH_4F and then dropwise to the previous solution's beaker. The pH of the solution was carefully governed to a value of 9.5. After 6 h of stirring, FTO nanoparticles formed a white opaque precipitate. The solution was filtrated and dried for 4 h at 60 °C. Three calcination heat-treatments were performed by placing 150 mg of noncalcined FTO powder in a tubular furnace for 4 h under air flow (200 mL min^{-1}) at 300 °C, 500 °C, and 700 °C. Then, a modified polyol method was used to support IrO_2 salt precursor − $IrCl_3xH_2O$ (Alfa Aesar)—onto the prepared FTO powder in an ethane-1−2-diol solution (pH = 13), with an initial ratio of 1:1 wt % between the precursor and the support at 175 °C for 3 h. The final solution was filtrated and thoroughly washed using 1.5 L of ultrapure water to remove Cl^- ions. The collected IrOx-based nanoparticles were dried in an oven at 100 °C for 5 h.

A commercial Ir oxide powder (IrO_2, 99.99% trace metals basis, Premetek, P40 V020 − 10−20 m^2 g^{-1}) was used to benchmark the OER activity of the synthesized catalysts and to assess the differences in morphological structure and composition. These nanoparticles were employed as supplied; therefore, they were not subjected to any annealing step.

2.2. Physicochemical Characterization

X-ray dispersion (XRD) was used to evaluate the crystallinity of the IrO_2-based electrocatalysts at INL. The X-ray patterns were retrieved using a PANanalytical X'Pert Pro operating in Bragg−Bretano focusing geometry using Cu Kα radiation at wavelengths Cu Kα1 = 1.5406 Å and Cu Kα2 = 1.54443 Å.

The XPS spectra of all samples were obtained at DLR using an ultrahigh vacuum (UHV) setup with a base pressure of 2×10^{-10} mbar. The apparatus has a monochromatic AlKα (1486.74 eV) X-ray source, a delay-line detector, and a hemispherical electron energy analyzer (SPECS Phoibos 150). High-resolution spectra were obtained at a typical emission takeoff angle and a pass energy of 20 eV, yielding an overall experimental peak broadening of 0.5 eV. After subtracting the Shirley background, all core-level spectra were fitted using the commercially available CasaXPS program (www.casaxps.com). The constraints placed on the peak spacing and peak area ratios of the Ir 4f7/2 and Ir 4f5/2 components were 3 eV and 4:3, respectively, for all fits.

Thermogravimetric analysis (TGA) was performed using a thermogravimetric analyzer (TG 209 F1 Iris, NETZSCH) under 30 cm^3 min^{-1} of airflow and heating from room temperature to 1000 °C at 2 °C min^{-1}. (10 ± 1) mg of catalyst powder was used in each analysis.

The Ir mass fractions of the prepared catalysts were determined using inductively coupled plasma−optical emission spectroscopy (ICP-OES; Thermo iCAP 7000). A sample of 10 mg of each catalyst was dissolved in 10 mL of aqua regia at 100 °C. A thermogravimetric analyzer (TG 209 F1 Iris, NETZSCH) was also utilized to evaluate the thermal behavior of the prepared catalysts in an oxidative environment (O_2) between room temperature and 900 °C.

The bulk elemental composition of the IrO_x/FTO catalysts was analyzed by energy-dispersive X-ray spectroscopy (EDS), which was integrated into a Phenom ProX desktop scanning electron microscope (SEM). The latter was equipped with a field-emission source. Images at several magnifications were captured using a backscatter electron detector and a secondary electron detector while operating under a high vacuum and at an accelerating voltage of 15 kV.

The X-ray absorption spectroscopy (XAS) was carried out at the BL22-CLAESS beamline at the ALBA Synchrotron in Barcelona, Spain. For *ex situ* analysis (measured at the L_3-edge in transmission), 10 mg of catalysts was thoroughly ground with 70 mg of cellulose for 45 min and pressed (2 tons, 30 s), resulting in a pellet with a 10 mm diameter. Before the analysis, each pellet was placed between Kapton tape.

Samples for transmission electron microscopy (TEM) were prepared by dispersing the catalyst powder in a copper mesh, and the Ir particle sizes and their dispersion were evaluated by using a Jeol HEM 1400 TEM analyzer. The particle size of Ir nanoparticles was evaluated by using ImageJ software.

2.3. Electrochemical Characterization

2.3.1. Electrode Preparation and Conditioning. An Au tip of 0.196 cm^2 was used as working electrode after being polished with 1 μm diamond particle solution followed by a 0.05 μm alumina-particle solution. The catalyst suspension deposited on the Au tip consisted of 20 μL containing an overall mass of metallic iridium of 2.8 ± 0.1 μg_{Ir} (loading of 14.2 μg_{Ir} cm^{-2}). Immediately after dipping the working

Downloaded from pubs.acs.org/acsodf/article-pdf/11/44/69026/6903792/acsomega.6c08923.pdf by UNIVERSIDADE DO PORTO 01100 user on 25 November 2026

https://doi.org/10.1021/acsomega.6c08923
ACS Omega 2026, 11, 69026−69037

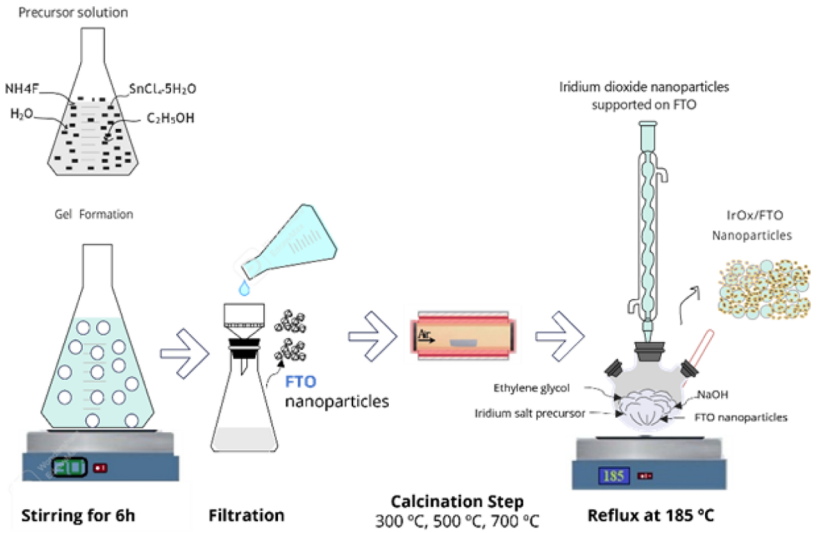

Figure 1. Synthesis route for the preparation of 30 wt % IrO_x supported on FTO nanoparticles.

electrode into the electrolyte (0.1 M $HClO_4$(aq)), the potential was controlled at 50 mV for 10 min under Ar saturation to reduce the reversible iridium oxide species that could have been formed during the catalyst synthesis procedure. The electrode was initially conditioned in Ar during 100 cycles between 0.05 V and 1.4 V (vs RHE) at 100 mV s^{-1} and 0 rpm.

2.3.2. OER Activity and Stability. The electrochemical impedance spectra were obtained in potentiostatic mode using a 10 mV perturbation at high frequency range (999 mHz−1 kHz) to measure the ohmic drop. The OER activity was measured while performing linear sweep voltammetry (between 1.1 V and 1.8 V vs RHE at 20 mV s^{-1}) at 1600 rpm in Ar saturated electrolyte. During the measurements, a gas blanketing was set to prevent electrolyte contamination from the exterior of the cell. A cyclic voltammogram (CV) was recorded from 0.05 to 1.4 V using a scan rate of 20 mV s^{-1}. Afterward, a linear sweep voltammetry (LSV) was recorded from 1.1 to 1.9 V vs RHE at 1600 rpm to ascribe the OER mass activity of each catalyst.

The electrochemically active surface area (ECSA) was determined based on the electrochemical double-layer capacitance (C_{dl}), acquired by carrying out cyclic voltammograms at different scan speeds within the nonfaradaic region from 1.20 to 1.40 V_{RHE}. This approach was chosen due to the established proportionality between ECSA and C_{dl} for a given material, as expressed by the equation $C_{dl} = i_c/\nu$. Here, C_{dl} represents the double-layer capacitance of the electroactive material in Farads per square centimeter (mF cm^{-2}), while i_c and ν denote the charging current in milliamperes per square centimeter (mA cm^{-2}) and the scan rate in millivolts per second (mV s^{-1}), respectively. An accelerated stress test was performed to assess the stability of the electrocatalyst while performing the OER. In this regard, the working electrode endured 10 000 cycles between 1.1 and 1.8 V_{RHE} at a scan rate of 100 mV s^{-1}, while maintaining the electrode rotation at 1600 rpm to avoid accumulating O_2 bubbles. Electrochemical impedance spectroscopy (EIS), linear sweep voltammetry (LSV), and CV were recorded again to assess the reproducibility of the results.

2.3.3. Electrochemically Active Surface Area by Cu Underpotential Deposition. As a separate experiment, the copper underpotential deposition (Cu-UPD) method was employed as a comparative electrochemical probe of the accessible Ir-containing surface of the synthesized electrocatalysts. First, the electrode was kept in a purged (Ar) 0.1 M H_2SO_4 electrolyte at 0.05 V vs RHE for 10 min to reduce the reversible iridium oxide species formed during the synthesis of the catalysts. The electrode was cycled in the potential range from 0.2 to 0.72 V vs. RHE at 20 mV s^{-1} to obtain a first background CV, followed by a second electrode reduction of 15 min at 0.05 V. The first electrolyte was then replaced by another containing 0.5 M H_2SO_4 and 5 mM of Cu_2SO_4 (Merck), and it was purged again with Ar for half an hour. Afterward, the electrode was cycled for 5 times (0.2 to 0.72 V vs. RHE at 20 mV s^{-1}) to retrieve the Cu-UPD voltammogram.

The integrated Cu stripping charge was used as a comparative measure of the electrochemically accessible Ir-containing surface. Although Cu-UPD is commonly employed to estimate the surface area of metallic noble metals, the adsorption stoichiometry and coverage of Cu on mixed-valence IrO_x surfaces may differ from those established for metallic Ir. Moreover, Cu deposition on the conductive FTO support cannot be completely excluded. Therefore, the Cu-UPD charge was not converted to an absolute ECSA based on an assumed 1:1 Cu/Ir surface stoichiometry. Instead, the Cu-UPD results were used to compare the relative electrochemical accessibility of the Ir-containing phase among the investigated catalysts under the identical experimental conditions.

2.3.4. Membrane Electrode Assembly Fabrication and Single-Cell Testing. *2.3.4.1. Fabrication and Characterization of CCMs in a PEMWE Single Cell.* A catalyst ink was prepared by mixing the synthesized powders of IrO_x/FTO and the commercial Pt/C|IrO_2, together with 8 mL ultrapure water (Milipore), 2 mL of 2-propanol (Sigma-Aldrich, 99.9%); Nafion suspension (5 wt %, Quintech) was added in a ratio of ionomer-to-carbon mass ratio = 30 wt %. To create catalyst-coated membranes (CCM) with 1 mg $_{catalyst}$ cm^{-2} at the anode side and 0.3 mg_{Pt} cm^{-2} at the cathode side using Ir-based catalysts, the ink was sprayed on both sides of a Nafion 115 membrane. Two Ti porous transport layers with Pt coating, hydrophilic carbon paper (Sigracarb 2050, Fuel Cell Store) at the cathode side, and each constructed CCM positioned in the center, were used to create a PEM water electrolyzer (4 cm^2). Four screws were tightened to a torque of 0.6 N m to fasten the cell.

Each PEM electrolyzer containing the prepared CCMs was characterized by performing 5 polarization curves at 60 °C using a slew rate of 10 mV s^{-1}, and by retrieving electrochemical impedance spectra in galvanostatic mode (8 A). To assess the stability of the best performing system, a chronopotentiometry was performed at 1.3 A cm^{-2} for 320 h and 80 °C.

3. RESULTS AND DISCUSSION

3.1. Preparation and Morphological Characterization of the Prepared Ir/FTO Catalysts

A facile and scalable sol−gel method synthesized FTO nanoparticles with a narrow particle size distribution of 40−80 nm. These nanoparticles were then subjected to different annealing temperatures to optimize their properties; they were subsequently nucleated with minimal loadings of iridium salt

Downloaded from pubs.acs.org/acsodf/article-pdf/11/44/69026/6903792/acsomega.6c08923.pdf by UNIVERSIDADE DO PORTO 01100 user on 25 November 2026

https://doi.org/10.1021/acsomega.6c08923
ACS Omega 2026, 11, 69026−69037

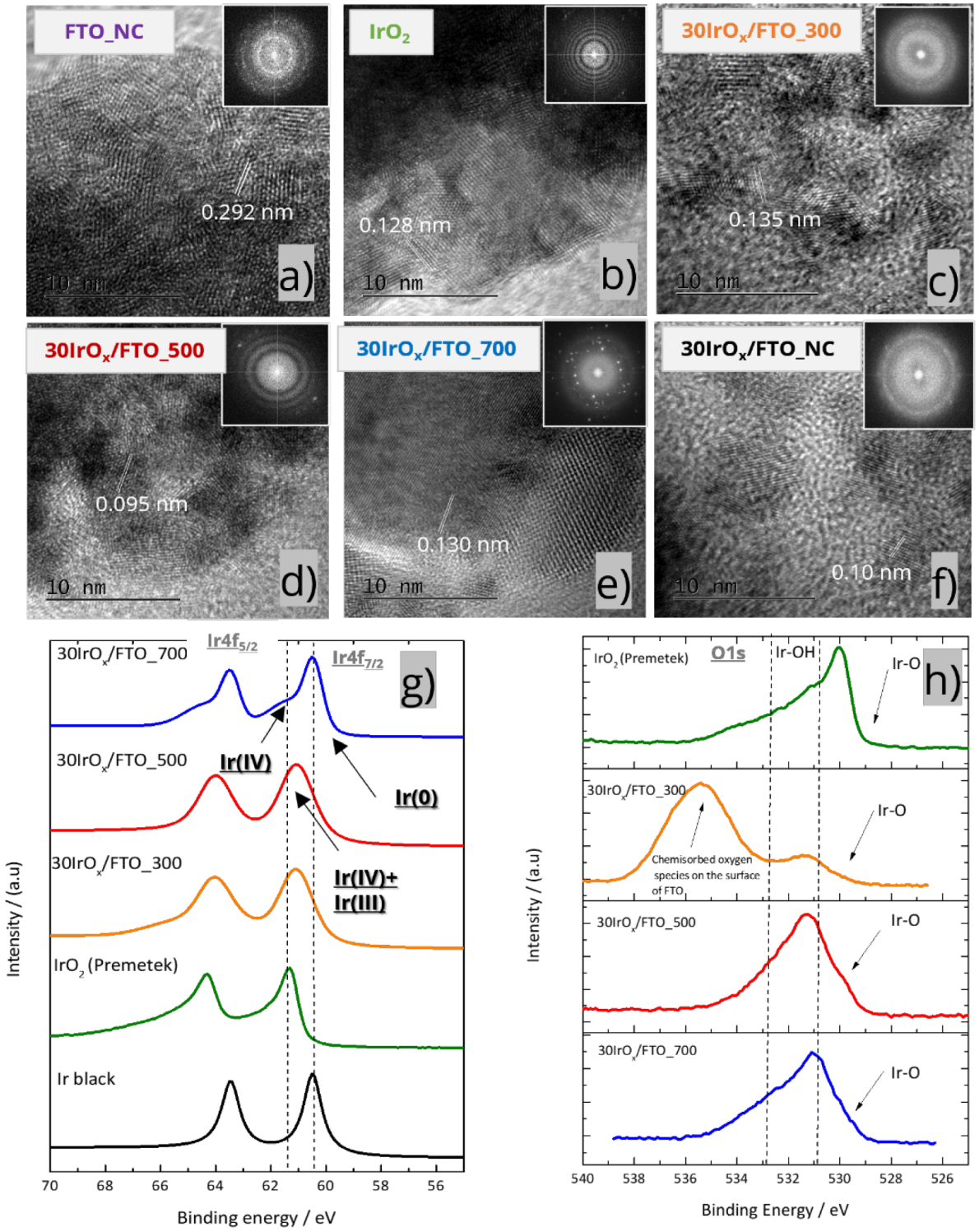

Figure 2. HR-TEM images of a) FTO_NC, b) IrO_2, c) IrO_x/FTO_300, d) IrO_x/FTO_500, e) IrO_x/FTO_700, f) IrO_x/FTO_NC, and the respective XPS spectra for g) Ir 4f and h) O 1s regions. The insets in images (a) to (f) show the SAED patterns of the supported catalysts.

precursor using a modified polyol method (Figure 1). FTO nanoparticles were obtained after annealing the sol−gel precursor under airflow at 300 °C, 500 or 700 °C for 5 h (referred to in the text as FTO_300, FTO_500, and FTO_700, respectively). The resulting nanoparticles present different average particle sizes and colors, as seen in Figure S1. The color was assigned to the different oxidation states of tin. An aliquot of the as-prepared, noncalcined FTO nanoparticles (FTO_NC) was stored for use as a reference support.

Subsequently, iridium nanoparticles were nucleated onto the prepared FTO nanoparticles using a modified polyol method. During this process, the hydroxyl groups (−OH) of ethylene glycol served dual roles as both solvent and reducing agent for the iridium salt precursor, $IrCl_3{\cdot}xH_2O$, resulting in the formation of 30 wt % IrO_x/FTO_Y nanoparticles, where Y

https://doi.org/10.1021/acsomega.6c08923
ACS Omega 2026, 11, 69026−69037

Downloaded from pubs.acs.org/acsodf/article-pdf/11/44/69026/6903792/acsomega.6c08923.pdf by UNIVERSIDADE DO PORTO 01100 user on 25 November 2026

represents the annealing temperature (300, 500, or 700 °C). The Ir mass loading of prepared catalysts was determined by inductively coupled plasma−mass spectroscopy (ICP-MS), and the obtained results indicate an average mass fraction of 27−30 wt % (Table S1). The morphology of the produced nanoparticles was unveiled by high-resolution transmission electron microscopy (HR-TEM, Figure 2a−f) and the crystallinity/structure of selected areas by electron diffraction (SAED) (insets from Figure 2a−f). The direct measurement of the spacing between crystal fringes yields a d(hkl) value of approximately 2.9 Å for FTO_NC nanoparticles and approximately 0.95 Å to 1.35 Å for IrO_x/2-based catalysts. These values correspond to the lattice spacing of (110), (101), and (220) family planes of IrO_2 (PDF No. 150870). From the SAED insets, the bright dotted reflection rings of the commercial IrO_2 suggest high crystallinity, which is often assigned to rutile-type crystal structures (inset of Figure 2b);[18] the remaining SAED patterns of the supported IrO_x/FTO nanoparticles reveal mostly diffused continuous, thick diffraction rings typical amorphous IrO_x (Figure 2c,d,f).[19] When calcined at higher temperatures, the FTO supports exhibit increasingly sharper ring reflections in the SAED patterns, which indicate improved crystallinity of Ir and larger average Ir grain size. Scanning electron microscopy (SEM) images of as-prepared noncalcined FTO samples (FTO_NC) reveal well-ordered parallelepiped-shaped particles of various sizes (Figure S2a) exhibiting a characteristic crystalline morphology. Additionally, the observation of strong diffraction rings (Figure 2a) confirms a mild crystallinity of the FTO_NC structures. Observing both blurred and spaced strong rings in the SAED pattern (IrO_x/FTO_700, Figure 2e) suggests the coexistence of both amorphous and crystalline phases in the catalyst annealed at 700 °C.[18] This variation in phase distribution may arise from nonuniform distributions of elements and incomplete ordering of atoms during the annealing step and subsequent polyol chemical reaction, particularly for F^- ions and Ir^{2+} ions, respectively. However, defects in metal oxide catalysts are generally more prevalent at higher temperatures, beyond 1000 °C, where fully polycrystalline structures are typically formed.[20]

From low-resolution (LR) TEM images, the commercial IrO_2 nanoparticles (Figure S3a) own a distinct tetragonal structure (typical of rutile IrO_2) and the average Ir particle size is much larger comparatively to when these particles are dispersed over FTO supports (from ca. 20 nm of IrO_2 to ca. 2 nm of IrO_x/FTO catalysts, Figure S3b-e). Ir oxyhydroxide particles' coarse and irregular edges observed in the supported IrO_x/FTO structures calcinated at <500 °C indicate an amorphous structure. In contrast, the presence of well-defined crystal lattice fringes in the sample calcinated at 700 °C confirms the moderate crystallinity of the iridium nanoparticles, approaching that of IrO_2 rutile type.[21] As the support annealing temperature increased, there was a slight tendency for the average size of Ir particles to increase, particularly for crystallization temperatures >500 °C (IrO_x/FTO_700, Figure S3e); crystallization is a thermally activated process, and at elevated temperatures, nanoparticles tend to grow and coalesce into larger, more stable structures.

TG curves (Figure S4) corroborate the enhanced crystallinity of the IrO_x/FTO_700 catalyst. The IrO_x/FTO_700 catalyst desorbs physiosorbed water at significantly higher temperatures, further supporting its increased crystallinity. This observation is consistent with the observation that crystalline structures typically exhibit stronger adsorption sites.[22] IrO_x/FTO_700 exhibits a low mass loss of about 1.5 wt % at 200−300 °C, whereas more amorphous structures have a fast mass loss of approximately 6 wt % at ca. 100 °C.

XPS was used to determine the valence states and surface chemical composition of the prepared supported and/or annealed samples, as shown in Figure 2g,h. The analyzed regions for Sn (3d) and Ir (4f) of the prepared catalysts display spaced doublets due to *j-j* spin−orbit coupling[23] (Figure s2g and S5). The Ir_{4f} lines display a shift of the $4f_{7/2}$ peak toward lower binding energy (BE) with increasing annealing temperatures of the support (ca. 60.9 eV, IrO_x/FTO_700), unveiling particularly larger contributions of Ir(IV) species as well as metallic Ir (Ir^0)[24−26] for the sample annealed at 700 °C (IrO_x/FTO_700; Figure S6 and Tables S2).

The Ir 4f line for the Ir black sample is noticeably asymmetric, typical of highly metallic conductors, and well characterized by a straightforward Doniach-Sunjic function.[27] It has been proposed that the coexistence of the hybrid Ir valence states, Ir(III) and Ir(IV), as well as the concomitant surface species, such as electrophilic O^- species, is necessary to have intrinsic OER activity on amorphous IrO_x samples.[28] The existence of multiple iridium oxidation states is mostly observed for samples calcined at 300 and 500 °C (Figure S6); compared with the commercial IrO_2 sample, samples calcined at 300 and 500 °C are more prone to display a more amorphous structure—broader Ir 4f line, from 60 to 61.5 eV region—mainly due to the presence of Ir(III) species in the matrix.

The similar shapes of both spectra (IrO_x/FTO_300, IrO_x/FTO_500), characterized by symmetrical and mostly overlapping peaks, are indicative of amorphous IrO_x-based samples,[23,29] suggesting a similar composition of both composites. Additionally, the higher ratio of species Ir(III) and Ir(IV) ($R_{III/IV}$) at the surface of IrO_x/FTO_500 catalyst (approximately 4 times higher than the sample calcined at 700 °C) suggests a stronger metal−support interaction and, consequently, charge transfer from the support to the catalyst (Figure S7).

The O 1s regions of the samples reveal a consistent pattern. The strong resonances at 530 and 533 eV of the commercial IrO_2 sample align well with the expected O 1s line spectrum of rutile-type IrO_2 catalysts (Figure 2h);[25] this is further supported by Figure S6. For samples IrO_x/FTO_300 and IrO_x/FTO_500, a more prominent and broader resonance peak emerges at 531−532 eV, indicating the coexistence of both O^- and O^{2-} species, which is typically observed in amorphous IrO_x spectra.[25] Furthermore, the higher BE values observed for the O 1s line of sample IrO_x/FTO_300 were assigned to some adventitious oxygen from the polyol process adsorbed on top of the support.[30] The substitution of F^- ions for O^{2-} in the SnO_2 lattice structure induces substantial changes in both the O 1s and Sn 3d peaks (Figures S5 and S6). These changes are primarily due to the formation of oxygen vacancies and surface defects, which are generated by incorporating F^- ions into the SnO_2 lattice.[31,32] As the annealing/calcination temperature of the support increases (from 300 to 700 °C), the O 1s and Sn 3d spectra shift toward lower binding energies, indicating a gradual increase in crystallinity.[30] The stoichiometric substitution of a divalent oxide (O^{2-}) requires the incorporation of two monovalent fluoride (F^-) ions to ensure charge balance. This facile substitution of O^{2-} by two F^- ions occurs because the

Downloaded from pubs.acs.org/acsodf/article-pdf/11/44/69026/6903792/acsomega.6c08923.pdf by UNIVERSIDADE DO PORTO 01100 user on 25 November 2026

https://doi.org/10.1021/acsomega.6c08923
ACS Omega 2026, 11, 69026−69037

electronegativity of F^- ($\chi F^- \approx 4.368$) is significantly higher than that of O^{2-} ($\chi O^{2-} \approx 3.758$), and the ion radius difference between F^- and O^{2-} ($rO^{2-} \approx 1.40$ Å, $rF^- \approx 1.33$ Å) is negligible.[33] The open oxygen positions in the SnO_2 lattice are occupied by these fluorine ions. Moreover, the electrocatalyst annealed at 500 °C shows a larger ratio between O^{2-} and lattice oxygen than the electrocatalysts annealed at lower temperatures, as shown in Figure S8 for IrO_x/FTO_500. The excess presence of O^{2-} has been attributed to its crucial role in expanding the electron transfer pathways from the support to the active catalyst through a charge replenishment mechanism, thereby maintaining the most active Ir(III) states.[34] XPS spectra reveal F 1s signals at 690−693 eV, confirming the presence of fluorine in the near-surface region of the FTO nanoparticles. The corresponding XPS quantification yielded a fluorine concentration of (2.6 ± 0.4) wt %. The observed F signal is consistent with the incorporation of fluorine into the SnO_2-based FTO structure, although the XPS-derived value should be regarded as a near-surface concentration rather than a bulk fluorine content (Figures S5 and S9).

The XRD pattern for the prepared FTO nanoparticles does not show any identifiable peak, suggesting that either the support is composed of very small nanoparticles (<2 nm) or it is amorphous. Since TEM characterization indicates an FTO particle size of 20−40 nm, the XRD pattern of synthesized FTO indicates that low crystallinity was achieved after the sol−gel process. It should be emphasized that crystallinity observed by TEM might be due to electron beam degradation as reported in the literature. No changes on the XRD pattern were observed after adding Ir for the noncalcined sample, indicating that the Ir sites were well dispersed throughout the support as either single metallic sites, clusters, or very small nanoparticles. After annealing at 300 °C, peaks related to tetragonal SnO_2 (JCPDS 005−0467) evolved, while no distinct peaks for IrO_2 (JCPDS card no. 15870) are observed. The lack of peaks, apart than these assigned to SnO_2, suggests that F remained within the main phase structure, and hence no phase segregation occurred. It also suggests that the oxidation of Ir sites, as indicated by XPS, did not translate on severe agglomeration. Heat treatment performed on other supported Ir-based catalysts, such as Ir/ATO or Ir/ITO, leads to the formation of rutile IrO_2 at ca. 450 °C. However, no significant changes were observed after annealing at 300 or 500 °C as seen in Figure 3a, indicating that IrO_2 NPs remain well dispersed and with a small particle size (<2 nm) as confirmed by TEM; the latter might be due to the strong metal oxide-support interaction that limits particle agglomeration. For comparison, the XRD spectra for commercial IrO_2 can be found in Figure S10.

To further elucidate the oxidation state of Ir species in IrO_x/FTO_500, which exhibited promising OER activity, X-ray absorption spectroscopy (XAS) analysis was employed to assess the Ir-L3 edge (Figure 3b). Ir black, IrO_2, and $IrCl_3$•xH2O were also analyzed for comparison purposes. The overall oxidation state was determined by examining the white line (WL) position, corresponding to the first absorption edge in the X-ray absorption near-edge structure (XANES) region. The WL line for Ir black and rutile IrO_2 was centered at 11216.4 and 11218.2 eV, respectively. The WL energy for $Ir^{III}Cl_3$ was 11216.9 eV, indicating the presence of both Ir(III) and Ir(IV) species, with Ir(III) being the predominant oxidation state.[35] Notably, the WL position for IrO_x/FTO_500 was found at 11217.4 eV, intermediate between Ir

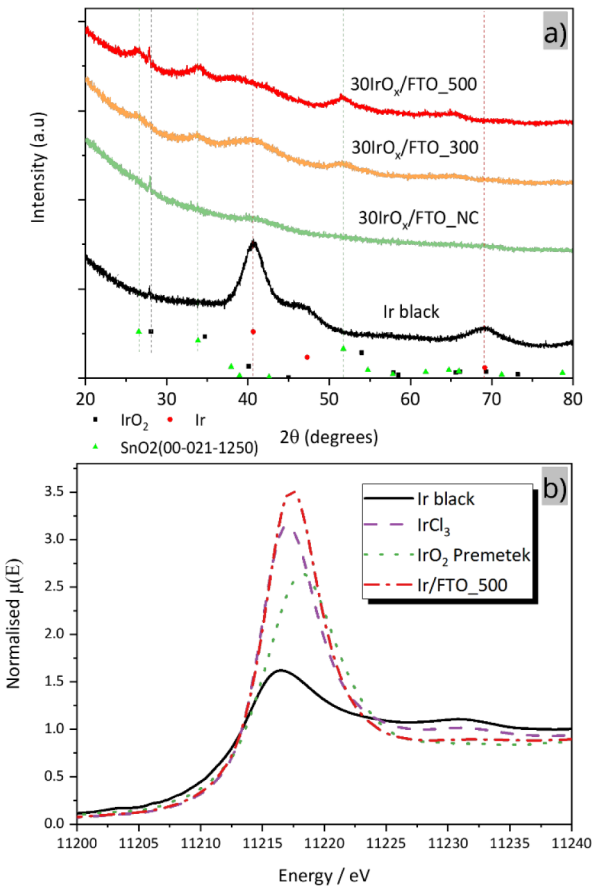

Figure 3. (a) X-ray diffraction (XRD) patterns a) of Ir black, 30IrO_x/FTO_Y (Y = 500, 300, NC) samples and X-ray absorption spectra (XAS) b) of Ir black, IrO_2, salt precursor $IrCl_3$ and 30IrO_x/FTO_500.

black and IrO_2, confirming the coexistence of Ir^{3+} and Ir^{4+} sites both at the surface and within the bulk. These WL intensity and energy differences suggest substantial structural and morphological variations between the samples, including oxidation state, local structure, and particle size.[36]

Although N_2 physisorption measurements were not performed, the morphological evolution observed by TEM/SEM and the increasing crystallinity revealed by XRD/SAED indicate progressive structural consolidation of the FTO nanoparticles with increasing annealing temperature. In particular, the larger particle size observed for FTO_700 suggests a reduction in the physical surface area upon high-temperature treatment. Nevertheless, the electrochemically accessible surface area of the resulting IrO_x/FTO catalysts is governed by several additional factors, including IrO_x dispersion, particle size, oxidation state, and metal−support interactions.

3.2. OER Mass Activity and Stability

The OER activity of the prepared catalysts was assessed using a conventional thin film rotating disc electrode (RDE) setup, in a 0.1 M $HClO_4$(aq) solution at room temperature, as shown in Figure 4a. The OER onset occurs between *ca.* 1.49 V_{RHE} and 1.6 V_{RHE} for j = 1 mA cm^{-2}. While all synthesized electrocatalysts exhibited superior OER activity compared to the commercial IrO_2 catalyst, IrO_x/FTO_300 displayed a notable decrease in activity. XPS analysis revealed a significantly higher chemisorbed oxygen content on the surface of catalyst sample IrO_x/FTO_300 (Figure 2h). This excessive

Downloaded from pubs.acs.org/acsodf/article-pdf/11/44/69026/6903792/acsomega.6c08923.pdf by UNIVERSIDADE DO PORTO 01100 user on 25 November 2026

https://doi.org/10.1021/acsomega.6c08923
ACS Omega 2026, 11, 69026−69037

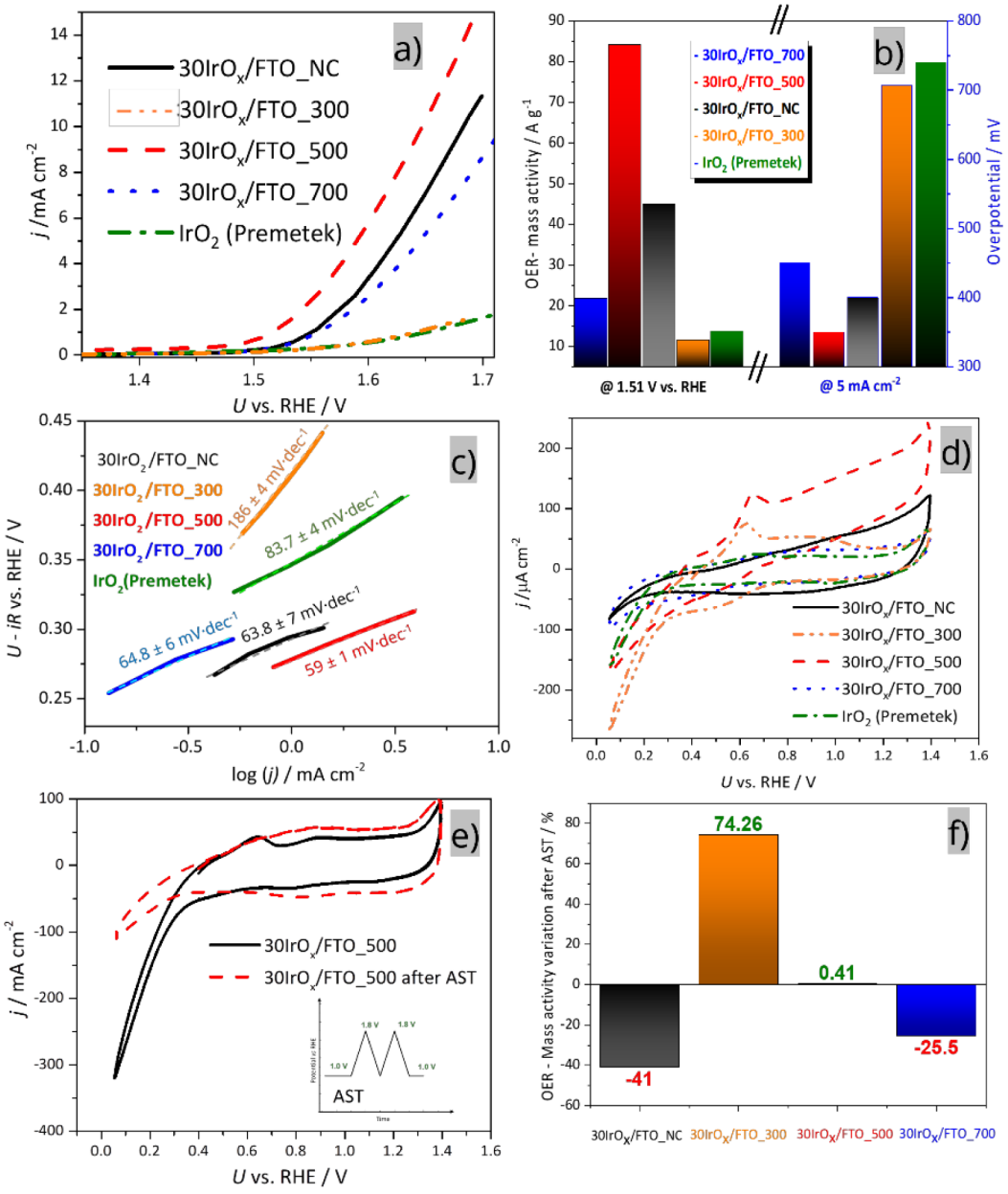

Figure 4. RDE characterization of $30IrO_x$/FTO_Y (Y = NC, 300 °C, 500 or 700 °C) and IrO_2 by means of a) OER LSVs recorded at 2 mV s^{-1}; b) OER mass activity at 1.51 V vs RHE and overpotential at j = 5 mA cm^{-2}; and c) Tafel plots measured at 2 mV s^{-1}. d) CVs at beginning of life and e) BoL and end of life (EoL) after accelerated stress test (AST) of 10k cycles for IrO_x/FTO_500 recorded at 20 mV s^{-1} in an Ar saturated 0.1 M $HClO_4$ solution at 25 °C. f) OER mass activity variation upon intensive cycling of each synthesized catalyst—measurements at 1.51 V_{RHE}; the loading of Ir catalyst was 14.2 μg_{Ir} cm^{-2} in the 0.196 cm^2 Au WE tip at 1600 rpm.

oxygen coverage is believed to hinder water adsorption and access to the active sites, thereby suppressing OER activity.[37] Still, the overpotential measured at 5 mA cm^{-2} for all the prepared catalysts is significantly lower than for IrO_2 – Figure 4b.

The prepared IrO_x/FTO_500 catalyst displays the most negative onset potential and thus the highest OER mass activity (MA) at 1.51 V_{RHE}, delivering a 5.5-fold higher OER MA compared to the commercial counterpart (85 A g^{-1} vs 15.5 A g^{-1} at 25 °C, respectively, at 1600 rpm). The coexistence of crystalline and amorphous regions in the catalyst IrO_x/FTO_500 is believed to be crucial in its enhanced OER mass activity.[34,38] Crystalline areas offer precise active sites with defined structures, while amorphous regions enhance surface area and reactivity, promoting efficient reactant and product movement.

The Tafel slope of each catalyst was subsequently measured within the overpotential window of 250 mV < η < 450 mV (Figure 4c). All overpotential values were adjusted using jR-correction to compensate for the electrolyte resistance. The smallest Tafel slope was achieved for catalyst IrO_x/FTO_500 with solely 59 mV dec^{-1}, followed by catalyst IrO_x/FTO_NC with 63.8 mV dec^{-1}, catalyst IrO_x/FTO_700 with 64.8 mV dec^{-1}, catalyst IrO_2 with 83.4 mV dec^{-1} and catalyst IrO_x/FTO_300 with 186 mV dec^{-1}. The determined Tafel slope for the commercial catalyst is within the usually reported range, i.e., 83.7 mV dec^{-1};[39,40] the smaller Tafel slopes observed for

https://doi.org/10.1021/acsomega.6c08923
ACS Omega 2026, 11, 69026−69037

Downloaded from pubs.acs.org/acsodf/article-pdf/11/44/69026/6903792/acsomega.6c08923.pdf by UNIVERSIDADE DO PORTO 01100 user on 25 November 2026

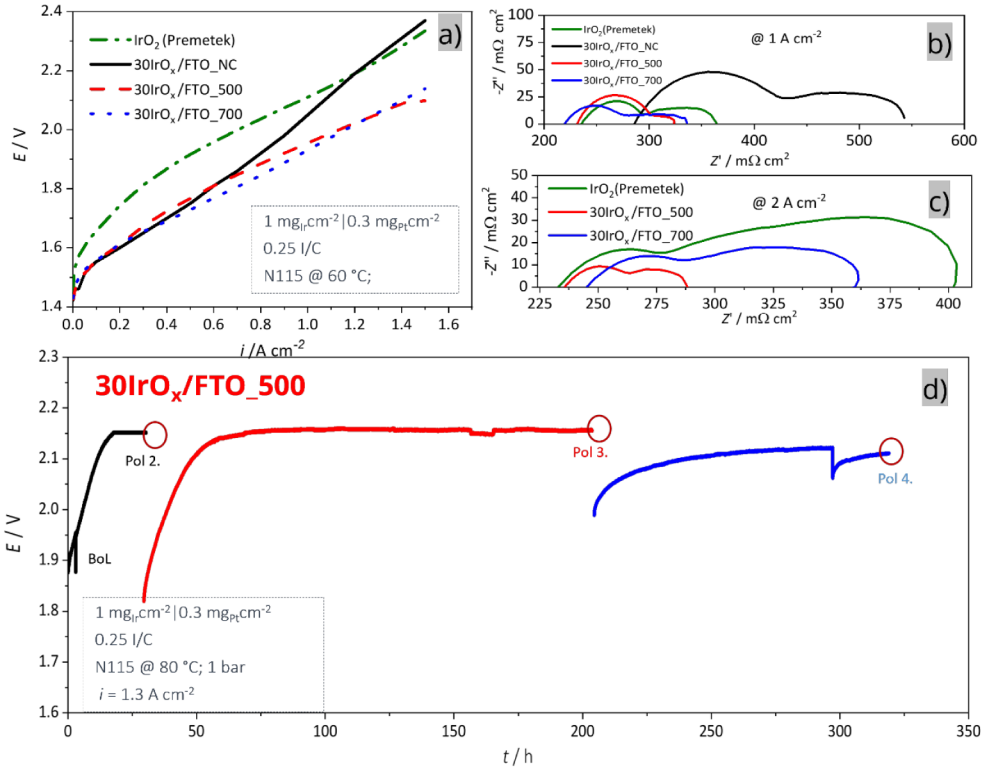

Figure 5. Electrochemical data of several PEMWE encompassing anodes composed of IrO_x supported catalysts on FTO_Y (Y= 300 °C, 500 °C, 700 °C) or commercial IrO_2 catalyst: a) polarization curves of PEMWE single cell with demineralized water at 60 °C; EIS spectra recorded b) at 1 A cm^{-2} and at c) 2 A cm^{-2} at 60 °C; d) chronopotentiometry data for stability test of 30IrO_x/FTO_500 in PEMWE single cell at 1.3 A cm^{-2} and 80 °C.

most of the prepared catalysts, on the other hand, confirm they're faster and more favorable kinetic toward OER.[41,42]

Figure 4d illustrates the CVs recorded at 20 mV s^{-1} for all prepared and commercial electrocatalysts, revealing distinct Ir valence states depending on the support material. The CVs generally exhibit a mirror-like rectangular shape, indicating good reversibility. Among the prepared catalysts, IrO_x/FTO_500 and IrO_x/FTO_300 exhibit the most pronounced quasi-reversible oxidation−reduction peaks on both positive and negative sweep directions, likely due to the presence of Ir(II)/Ir(III) complexes.[43] Interestingly, the redox transition from Ir(III)/Ir(IV) is consistently observed at *ca.* 0.97−1.0 V_{RHE} for all catalysts.[43] Despite its inferior OER activity, catalyst IrO_x/FTO_300 demonstrated a remarkable HER performance, with a current density of ∼300 mA cm^{-2}, surpassing the commercial IrO_2 catalyst by up to 3.5 times. The electrochemical active area (ECSA) of catalyst IrO_x/FTO_500, which is directly proportional to the electrical double layer charge (C_{dl}), is 2.97 mF cm^{-2}, exceeding that of catalyst IrO_x/FTO_300 by 1.5 times (Figure S11).[42,44] These findings indicate that the superior OER performance of IrOx/FTO_500 is associated, at least in part, with its higher electrochemically accessible surface area. However, the ECSA reflects the accessibility of the Ir-containing active phase and cannot be directly correlated with the specific surface area of the FTO support in the absence of quantitative physisorption measurements.

The long-term stability of the prepared catalysts was assessed based on an accelerated stress test (AST), comprising 10 000 cycles in the potential range of 1.1−1.8 V_{RHE} at a scan rate of 100 mV s^{-1}. Both the initial CVs and those obtained after the AST are shown in Figure S11a-d. After intense cycling, the Ir(II)/Ir(III) peaks were predominantly replaced by more oxidized species, particularly Ir(III)/Ir(IV), with a higher proportion of Ir(III) species observed for catalyst IrO_x/FTO_500 (Figure 4e). However, the reduction in the double-layer capacity of catalysts IrO_x/FTO_NC and IrO_x/FTO_700 suggests the initiation of degradation processes, as evidenced by a decrease in the peak current for the oxygen evolution. In contrast, catalysts IrO_x/FTO_500 and IrO_x/FTO_300 displayed mirror-like rectangular CVs after the AST, indicating enhanced reversibility and OER activity (Figure 4e). The increased charge below the peaks at ∼1.0 V RHE for both catalysts suggests an expansion of the active surface area, potentially attributable to eliminating impurities from the preparation procedure, such as Cl^- ions. These results are consistent with the OER-mass activity variations measured before and after the AST (Figure 4f).

The 30IrO_x/FTO300 catalyst exhibited a 74.26% increase in the OER mass activity after the AST. Although the removal of residual surface species, such as Cl-containing species originating from the Ir precursor, cannot be excluded, no direct evidence was obtained to confirm their removal. The observed activation may instead be associated with electrochemical restructuring and hydration of the IrO_x phase during potential cycling, leading to changes in its surface chemistry and an increase in the number of electrochemically accessible active sites. This interpretation is consistent with the structural evolution of IrO_x under repeated anodic polarization; however, complementary post-AST surface characterization would be required to confirm the proposed mechanism.

https://doi.org/10.1021/acsomega.6c08923
ACS Omega 2026, 11, 69026−69037

Downloaded from pubs.acs.org/acsodf/article-pdf/11/44/69026/6903792/acsomega.6c08923.pdf by UNIVERSIDADE DO PORTO 01100 user on 25 November 2026

No significant OER performance loss was detected for catalyst IrO_x/FTO_500, demonstrating its remarkable stability for water electrolysis operation. However, calcination at elevated temperatures (>500 °C) led to increased sintering of catalyst IrO_x/FTO_700, resulting in a 25.5% decline in OER-MA (Figure 4f). This observation highlights the importance of optimizing catalyst preparation conditions for high activity and stability. The best-performing catalyst in the present work was catalyst IrOx/FTO_500, calcinated at 500 °C with an FTO support also annealed at 500 °C.

3.3. PEMWE Performance

To validate the superior catalytic performance of catalyst IrO_x/FTO_500, a direct comparison with the commercial IrO_2 catalyst was conducted in a PEMWE single cell operated at 60 °C.

In contrast to catalyst IrO_2, all FTO-based anodes exhibited significantly lower overpotentials, particularly in the activation (200 mA cm^{-2}) and ohmic overpotential regions (Figure 5a). This improvement was attributed to the FTO nanoparticulated support, which enhances the in- and through-plane electrical conductivity of the catalytic layer. At 60 °C, the PEMWE system equipped with an anode made of catalyst IrO_x/FTO_500 reached a remarkable current density of 1.5 A cm^{-2} at 2 V, surpassing the commercial IrO_2 by 50%, which reached a current density of 700 mA cm^{-2}. Moreover, the anode made of catalyst IrO_x/FTO_500 enabled a substantial increase in Ir-specific power to 445 W g^{-1}_{Ir} at a cell efficiency of ca. 87%$_{HHV}$, corresponding to an operating potential of 1.6 V. In contrast, the IrO_2 catalyst only achieved a specific power of 75 W g^{-1} under the same conditions. These results demonstrate the superior catalytic performance of catalyst IrO_x/FTO_500. The anode made of the FTO calcined at 700 °C also exhibited an excellent performance, with remarkably low ohmic overpotentials, attributed to the more highly ordered lattice structure of crystalline metal oxide nanoparticles. The anode based on a noncalcined FTO support displayed larger mass transport overpotentials due to the significantly larger particle size of the metal catalytic particles, compromising both the water and gas management through the catalyst layer.

To additionally compare active areas (ECSA) between the commercial and the prepared anodes annealed at 500 and 700 °C, these anodes were subjected to a modified copper underpotential deposition (Cu-UPD) method to determine the electrochemical surface area (ECSA) in the single-cell configuration[19,45] (see Figures S13 and S14). Cu-UPD was employed as a comparative probe of the electrochemically accessible Ir-containing surface. The method is based on the adsorption of Cu on accessible Ir sites and the transfer of two electrons per adsorbed Cu atom during the stripping process.[45,46] Although this approach has been widely used for determining the surface area of metallic Ir, the Cu adsorption stoichiometry and coverage on mixed-valence IrO_x may differ from those reported for metallic Ir. Furthermore, a contribution from Cu deposition on the conductive FTO support cannot be completely excluded. Therefore, the Cu-UPD charge was used here to compare the relative electrochemical accessibility of the Ir-containing phase rather than to determine an absolute ECSA based on an assumed Cu monolayer.

The Cu-UPD stripping response obtained for the PEMWE equipped with the IrO_x/FTO_500 anode exhibited the highest charge density, reaching 1.6×10^{-3} C g^{-1} (Figure S12), approximately 1.6 times higher than that obtained for the commercial IrO_2 anode (Table S3). This higher Cu-UPD response indicates greater electrochemical accessibility of the Ir-containing phase in IrO_x/FTO_500 and is consistent with its superior OER mass activity at an overpotential of 280 mV (Figure 4b).

EIS measurements performed at 1 A cm^{-2} (Figure 5b) corroborated the observed trend. The charge transfer resistances associated with the OER for Ir catalysts dispersed over FTO nanoparticles (500 °C, 700 °C) were significantly lower compared to commercial IrO_2. Additionally, the corresponding anodes exhibited reduced ohmic resistances, falling below 230 mΩ cm^{-2}. At 2 A cm^{-2}, the anodes made of Ir dispersed on the FTO nanoparticles annealed at 500 °C exhibited the lowest mass-transport resistances (R_{diff}) of approximately 27.5 mΩ cm^{-2} (Figure 5c). This translates in a 3-fold overall cell resistance reduction when employing FTO_500 anodes, bringing the total resistance to 60 mΩ cm^{-2} compared to 180 mΩ cm^{-2} with the commercial IrO_2 catalyst. The lower ohmic resistance observed for the FTO-based MEAs may be associated with the increased structural ordering of the FTO support upon calcination, as evidenced by the XRD and TEM/SAED analyses. Nevertheless, the ohmic resistance obtained from EIS reflects the combined contributions of the catalyst layer, electrode interfaces, membrane, and other cell components. Since the electrical conductivity of the FTO powders was not independently measured, a direct correlation between FTO conductivity and the measured ohmic resistance cannot be established.

The long-term stability of the PEMWE equipped with the IrO_x/FTO_500 anode, was assessed through continuous chronopotentiometry at a fixed current density of 1.3 A cm^{-2} for over 320 h at 80 °C. During the initial stage of operation, the cell voltage increased from approximately 1.85 to 2.15 V within the first 40 h before reaching a relatively stable value. This initial voltage evolution is attributed to conditioning and equilibration of the MEA under the operating conditions, which may involve membrane hydration, ionomer and catalyst-layer wetting, changes in catalyst-layer/porous transport layer interfacial contact, and redistribution of water and gas transport pathways. Electrochemical restructuring or hydration of the IrO_x phase may also contribute to the observed behavior. However, as no time-resolved EIS or operando structural characterization was performed during this initial period, the individual contributions of these processes cannot be quantitatively distinguished. This study reveals a remarkable stability, with no significant and steady overpotential (η = 0.82 V) (Figure 5d). This stability contrasts with the degradation commonly reported for Ir-based catalysts in PEMWEs, where performance losses may arise from changes in the intrinsic OER activity, catalyst restructuring, electrochemically accessible surface area, and, in particular, Ir dissolution under harsh operating conditions.[19] In the present study, the IrO_x/FTO_500-based MEA maintained a stable cell potential during more than 320 h of operation at 1.3 A cm^{-2} and 80 °C, indicating excellent operational stability under the investigated conditions. Since Ir dissolution was not directly quantified, however, the present results do not allow to exclude gradual catalyst dissolution or redistribution within the MEA. Interestingly, after 320 h, the current density output of the cell even increased significantly, reaching 2 A cm^{-2} at 2 V (Figure S15). This observation suggests that the enhanced water−gas management was most likely attributed to favorable rearrange-

Downloaded from pubs.acs.org/acsodf/article-pdf/11/44/69026/6903792/acsomega.6c08923.pdf by UNIVERSIDADE DO PORTO 01100 user on 25 November 2026

https://doi.org/10.1021/acsomega.6c08923
ACS Omega 2026, 11, 69026−69037

ments within the catalyst layer microstructure, resulting in improved catalyst utilization.

The superior performance and stability of catalyst IrOx/FTO_500 were attributed to the enhanced interactions between the support, composed of annealed FTO nanoparticles (500 °C), and the Ir catalyst. During the OER process, typical Ir catalysts undergo oxidation from active Ir(III) state to Ir(IV) or Ir(V), leading to the formation of soluble intermediates and a gradual decrease in Ir solubility and catalytic activity. Annealing FTO at 500 °C facilitates the preservation of active Ir(III) species during long-term operation under harsh OER conditions, enabling a steady replenishment of charge. This mechanism contributes to both improved OER stability and electroactivity.[47]

4. CONCLUSIONS

This study shows that the preparation of Ir-based electrocatalysts with 30 wt % noble metal supported on fluorine-doped tin oxide (FTO) and annealed at 500 °C yields a highly active and stable catalyst for oxygen evolution in acidic environments.

The new supported catalyst exhibited a remarkable OER mass activity of ca. 85 A g^{-1}, surpassing the commercial iridium catalyst from Premetek by a factor of 6. Moreover, the as-prepared IrO_x/FTO_500 catalyst maintains a low OER overpotential of 320 mV at 5 mA cm^{-2} after completing an accelerated stress test of 10 000 cycles.

The remarkable stability enabled a 70% reduction in iridium loading in the anode of a PEMWE while simultaneously increasing the cell performance by 75% at 2 V, 60 °C. This translates to a nearly 4-fold higher Ir-specific power density compared to the commercial IrO_2 anode (440 W g^{-1} @ 87% $_{HHV}$). Furthermore, the optimized PEMWE exhibited exceptional stability for over 320 h at 1.3 A cm^{-2} and 80 °C conditions with negligible degradation (<0.001 mV dec^{-1}).

These findings highlight the potential of IrO_x/FTO_500 as a highly efficient and stable catalyst for low-cost commercial acid water electrolysis. Future work will focus on further reducing the iridium loading to values as low as 0.2 mg_{Ir} cm^{-2}, thus enhancing the practical application of this promising catalyst.

■ ASSOCIATED CONTENT

Supporting Information

The Supporting Information is available free of charge at https://pubs.acs.org/doi/10.1021/acsomega.6c08923.

Figure S1 - TEM images for FTO nanoparticles; Table S1 − ICP-MS measurements; Figure S2 − SEM images for FTO nanoparticles and IrO_x/FTO catalysts; Figure S3 − TEM images for IrO_x/FTO catalysts; Figure S4 − TEM images of commercial materials; Figure S5 − XPS spectra of prepared IrO_xbased electrocatalysts supported in FTO; Figure S6 − Fittings of Ir 4f spectra for IrO_x-based catalysts; Table S2 − Fit parameters; Figure S7 − TGA for IrO_x/FTO catalysts; Figure S8 - Fittings of O 1s spectra for IrOx-based catalysts; Figure S9 − XPS for O(1s) region; Figure S10 − XRD for commercial IrO_2rutile; Figure S11 − CVs of IrO_x/FTO catalysts; Figure S12 − CVs and Cu-UPD voltammograms; Figure S12 − Scheme of used hardware; Figure S14 − CVs before and after cycling; Table S13 − Surface iridium sites; Figure S15 − Polarization curve (PDF)

■ AUTHOR INFORMATION

Corresponding Authors

Andreas Friedrich − *Institute of Engineering Thermodynamics/Electrochemical Energy Technology, German Aerospace Center (DLR), Stuttgart 70569, Germany*; orcid.org/0000-0002-2968-5029; Email: andreas.friedrich@dlr.de

Adélio Mendes − *LEPABE − Laboratory for Process Engineering, Environment, Biotechnology and Energy, ALiCE − Associate Laboratory in Chemical Engineering, Faculty of Engineering, University of Porto, Porto 4200-465, Portugal*; orcid.org/0000-0003-2472-3265; Email: mendes@fe.up.pt

Authors

Sofia Delgado − *LEPABE − Laboratory for Process Engineering, Environment, Biotechnology and Energy, ALiCE − Associate Laboratory in Chemical Engineering, Faculty of Engineering, University of Porto, Porto 4200-465, Portugal*

Vincent Wilke − *Institute of Engineering Thermodynamics/Electrochemical Energy Technology, German Aerospace Center (DLR), Stuttgart 70569, Germany*

Rita Marques − *LEPABE − Laboratory for Process Engineering, Environment, Biotechnology and Energy, ALiCE − Associate Laboratory in Chemical Engineering, Faculty of Engineering, University of Porto, Porto 4200-465, Portugal*

Jonathan Ruiz Esquius − *Carbon Science and Technology Institute, INCAR-CSIC,, Oviedo 33011, Spain; Clean Energy Cluster, International Iberian Nanotechnology Laboratory, Braga 4715-330, Portugal*

Aldo Gago − *Institute of Engineering Thermodynamics/Electrochemical Energy Technology, German Aerospace Center (DLR), Stuttgart 70569, Germany*; orcid.org/0000-0001-7000-171X

Fátima Santos − *LEPABE − Laboratory for Process Engineering, Environment, Biotechnology and Energy, ALiCE − Associate Laboratory in Chemical Engineering, Faculty of Engineering, University of Porto, Porto 4200-465, Portugal*; orcid.org/0000-0002-9029-4107

Complete contact information is available at: https://pubs.acs.org/10.1021/acsomega.6c08923

Author Contributions

S.D.: Conceptualization, methodology, catalyst synthesis, XPS deconvolution, SEM analysis, CCM production, RDE testing, all cell experiments, and manuscript writing; V.W.: cell test screening at DLR; R.M.: XAS testing and manuscript writing (XAS); J.R.E.: XRD testing and manuscript reviewing; A.S.G.: supervision and manuscript reviewing; F.S.: manuscript reviewing. K.A.F.: supervision and manuscript reviewing. A.M.: main supervision and manuscript reviewing. All authors have read and agreed to the published version of the manuscript.

Notes

The authors declare no competing financial interest.

■ ACKNOWLEDGMENTS

This work is a result of Agenda "H2Driven Green Agenda", nr. C644923817-00000037, investment project nr. 50, financed by the Recovery and Resilience Plan (PRR) and by European Union - NextGeneration EU. This work was also supported by

Downloaded from pubs.acs.org/acsodf/article-pdf/11/44/69026/6903792/acsomega.6c08923.pdf by UNIVERSIDADE DO PORTO 01100 user on 25 November 2026

national funds through FCT/MECI: LEPABE, UID/00511/2025 (10.54499/UID/00511/2025) and UID/PRR/00511/2025 (10.54499/UID/PRR/00511/2025) and ALiCE, LA/P/0045/2020 (10.54499/LA/P/0045/2020). The authors acknowledge financial support from the EU Horizon 2020 FCH JU project NEWELY. The authors thank to Dr. Julia Müller-Hülstede and Dr. Indro Biswas from DLR for providing the HR-TEM measurements and XPS, respectively. The authors acknowledge financial support from the project Baterias 2030, reference POCI-01-0247-FEDER-046109, cofunded by the Operational Programme for Competitiveness and Internationalisation (COMPETE 2020), under the Portugal 2020 Partnership Agreement through the European Regional Development Fund (ERDF). Sofia Delgado and Rita Marques acknowledges FCT for the doctoral grant with reference SFRH/BD/144338/2019 and 2021.06496.BD, respectively. F.S. acknowledges the FCT for her research grant reference 2023.07366.CEECIND/CP2834/CT0012 (10.54499/2023.07366.CEECIND/CP2834/CT0012).

REFERENCES

(1) Marshall, A.; Børresen, B.; Hagen, G.; Tsypkin, M.; Tunold, R. Hydrogen production by advanced proton exchange membrane (PEM) water electrolysers—Reduced energy consumption by improved electrocatalysis. *Energy* **2007**, *32*, 431−436.

(2) Shirvanian, P.; van Berkel, F. Novel components in Proton Exchange Membrane (PEM) Water Electrolyzers (PEMWE): Status, challenges and future needs. A mini review. *Electrochem. Commun.* **2020**, *114*, 106704.

(3) Vesborg, P. C. K.; Jaramillo, T. F. Addressing the terawatt challenge: Scalability in the supply of chemical elements for renewable energy. *RSC Adv.* **2012**, *2*, 7933−7947.

(4) Feng, Q.; Yuan, X. Z.; Liu, G.; Wei, B.; Zhang, Z.; Li, H.; Wang, H. A review of proton exchange membrane water electrolysis on degradation mechanisms and mitigation strategies. *J. Power Sources* **2017**, *366*, 33−55.

(5) Siracusano, S.; Baglio, V.; Stassi, A.; Ornelas, R.; Antonucci, V.; Aric, A. S. Investigation of IrO2 electrocatalysts prepared by a sulfite-couplex route for the O2 evolution reaction in solid polymer electrolyte water electrolyzers. *Int. J. Hydrogen Energy* **2011**, *36* (13), 7822−7831.

(6) Lv, H.; Wang, S.; Li, J.; Shao, C.; Zhou, W.; Shen, X.; Xue, M.; Zhang, C. Self-assembled RuO2@ IrOx Core-Shell Nanocomposite as High Efficient Anode Catalyst for PEM Water Electrolyzer. *Appl. Surf. Sci.* **2020**, *514*, 145943.

(7) Van Pham, C.; Bühler, M.; Knöppel, J.; Bierling, M.; Seeberger, D.; Escalera-López, D.; Mayrhofer, K. J. J.; Cherevko, S.; Thiele, S. IrO_2 coated TiO_2 core-shell microparticles advance performance of low loading proton exchange membrane water electrolyzers. *Appl. Catal., B* **2020**, *269*, 118762.

(8) Zhao, F.; Wen, B.; Niu, W.; Chen, Z.; Yan, C.; Selloni, A.; Tully, C. G.; Yang, X.; Koel, B. E. Increasing Iridium Oxide Activity for the Oxygen Evolution Reaction with Hafnium Modification. *J. Am. Chem. Soc.* **2021**, *143*, 15616−15623.

(9) Liu, J.; Zhang, T.; Waterhouse, G. I. N. Complex alloy nanostructures as advanced catalysts for oxygen electrocatalysis: from materials design to applications. *J. Mater. Chem. A* **2020**, *8*, 23142−23161.

(10) Büchi, F. N.; Inaba, M.; Schmidt, T. J. *Polymer Electrolyte Fuel Cell Durability*; Springer New York, 2009. .

(11) Fabbri, E.; Schmidt, T. J. Oxygen Evolution Reaction—The Enigma in Water Electrolysis. *ACS Catal.* **2018**, *8*, 9765−9774.

(12) Wu, X.; Scott, K. RuO_2 supported on Sb-doped SnO_2 nanoparticles for polymer electrolyte membrane water electrolyzers. *Int. J. Hydrogen Energy* **2011**, *36*, 5806−5810.

(13) Marshall, A. T.; Haverkamp, R. G. Electrocatalytic activity of IrO_2−RuO_2 supported on Sb-doped SnO_2 nanoparticles. *Electrochim. Acta* **2010**, *55*, 1978−1984.

(14) Wang, L.; Song, F.; Ozouf, G.; Geiger, D.; Morawietz, T.; Handl, M.; Gazdzicki, P.; Beauger, C.; Kaiser, U.; Hiesgen, R.; Gago, A. S.; Friedrich, K. A. Improving the activity and stability of Ir catalysts for PEM electrolyzer anodes by SnO2: Sb aerogel supports: does V addition play an active role in electrocatalysis? *J. Mater. Chem. A* **2017**, *5*, 3172−3178.

(15) Solà-Hernández, L.; Claudel, F.; Maillard, F.; Beauger, C. Doped tin oxide aerogels as oxygen evolution reaction catalyst supports. *Int. J. Hydrogen Energy* **2019**, *44*, 24331−24341.

(16) Geiger, S.; Kasian, O.; Mingers, A. M.; Mayrhofer, K. J. J.; Cherevko. Stability limits of tin-based electrocatalyst supports. *Sci. Rep.* **2017**, *7*, 1−7.

(17) Manoj, B.; Raj, A. M.; Thomas, G. C. Tailoring of low grade coal to fluorescent nanocarbon structures and their potential as a glucose sensor. *Sci. Rep.* **2018**, *8* (1), 13891.

(18) Ortel, E.; Reier, T.; Strasser, P.; Kraehnert, R. Mesoporous IrO_2 Films Templated by PEO-PB-PEO Block-Copolymers: Self-Assembly, Crystallization Behavior, and Electrocatalytic Performance. *Chem. Mater.* **2011**, *23*, 3201−3209.

(19) Tan, X.; Shen, J.; Semagina, N.; Secanell, M. Decoupling structure-sensitive deactivation mechanisms of Ir/IrO_x electrocatalysts toward oxygen evolution reaction. *J. Catal.* **2019**, *371*, 57−70.

(20) Anwar, M.; Ghauri, I. M.; Siddiqi, S. A. An Xps Study Of Amorphous Thin Films Of Mixed Oxides In_2o_3−Sno_2 System Deposited By Co-Evaporation. *Int. J. Mod. Phys. B* **2007**, *21*, 1027−1042.

(21) Karimi, F.; Peppley, B. A.; Bazylak, A. Study of the Effect of Calcination Temperature on the Morphology and Activity of Iridium Oxide Electrocatalyst Supported on Antimony Tin Oxide (ATO) for PEM Electrolyser Technology. *ECS Trans.* **2015**, *69*, 87.

(22) Oh, S. H.; Nazar, L. F. Direct synthesis of electroactive mesoporous hydrous crystalline RuO_2 templated by a cationic surfactant. *J. Mater. Chem.* **2010**, *20*, 3834−3839.

(23) Ardizzone, S.; Bianchi, C. L.; Borgese, L.; Cappelletti, G.; Locatelli, C.; Minguzzi, A.; Rondinini, S.; Vertova, A.; Ricci, P. C.; Cannas, C.; Musinu, A. Physico-chemical characterization of IrO_2−SnO_2 sol-gel nanopowders for electrochemical applications. *J. Appl. Electrochem.* **2009**, *39*, 2093−2105.

(24) Wertheim, G. K.; Guggenheim, H. J. Conduction-electron screening in metallic oxides: IrO_2. *Phys. Rev. B* **1980**, *22*, 4680.

(25) Pfeifer, V.; Jones, T. E.; Velasco Vélez, J. J.; Massué, C.; Greiner, M. T.; Arrigo, R.; Teschner, D.; Girgsdies, F.; Scherzer, M.; Allan, J.; Hashagen, M.; Weinberg, G.; Piccinin, S.; Hävecker, M.; Knop-Gericke, A.; Schlögl, R. The electronic structure of iridium oxide electrodes active in water splitting. *Phys. Chem. Chem. Phys.* **2016**, *18*, 2292−2296.

(26) Minguzzi, A.; Lugaresi, O.; Achilli, E.; Locatelli, C.; Vertova, A.; Ghigna, P.; Rondinini, S. Observing the oxidation state turnover in heterogeneous iridium-based water oxidation catalysts. *Chem. Sci.* **2014**, *5*, 3591−3597.

(27) Pfeifer, V.; Jones, T. E.; Velasco Vélez, J. J.; Massué, C.; Arrigo, R.; Teschner, D.; Girgsdies, F.; Scherzer, M.; Greiner, M. T.; Allan, J.; Hashagen, M.; Weinberg, G.; Piccinin, S.; Hävecker, M.; Knop-Gericke, A.; Schlögl, R. The electronic structure of iridium and its oxides. *Surf. Interface Anal.* **2016**, *48*, 261−273.

(28) Minguzzi, A.; Locatelli, C.; Lugaresi, O.; Achilli, E.; Cappelletti, G.; Scavini, M.; Coduri, M.; Masala, P.; Sacchi, B.; Vertova, A.; Ghigna, P.; Rondinini, S. Easy Accommodation of Different Oxidation States in Iridium Oxide Nanoparticles with Different Hydration Degree as Water Oxidation Electrocatalysts. *ACS Catal.* **2015**, *5*, 5104−5115.

(29) Siracusano, S.; Baglio, V.; Grigoriev, S. A.; Merlo, L.; Fateev, V. N.; Aricò, A. S. The influence of iridium chemical oxidation state on the performance and durability of oxygen evolution catalysts in PEM electrolysis. *J. Power Sources* **2017**, *366*, 105−114.

Downloaded from pubs.acs.org/acsodf/article-pdf/11/44/69026/6903792/acsomega.6c08923.pdf by UNIVERSIDADE DO PORTO 01100 user on 25 November 2026

https://doi.org/10.1021/acsomega.6c08923
ACS Omega 2026, 11, 69026−69037

(30) Briggs, D. Surface and Interface Analysis. *Surf. Interface Anal.* **1981**, 3 (1), 1−1.
(31) Akkad, F. E.; Paulose, T. A. P. Optical transitions and point defects in F: SnO_2 films: Effect of annealing. *Appl. Surf. Sci.* **2014**, *295*, 8−17.
(32) Shewale, P. S.; Ung Sim, K.; Kim, Y.-B.; Kim, J. H.; Moholkar, A. V.; Uplane, M. D. Structural and Photoluminescence Characterization of SnO2: F Thin Films Deposited by Advanced Spray Pyrolysis Technique at Low Substrate Temperature. *J. Lumin.* **2013**, *139*, 113−118.
(33) Wang, X.; Wang, X.; Di, Q.; Zhao, H.; Liang, B.; Yang, J. Mutual Effects of Fluorine Dopant and Oxygen Vacancies on Structural and Luminescence Characteristics of F Doped SnO_2 Nanoparticles. *Materials* **2017**, *10* (12), 1398.
(34) Lee, G. R.; Kim, J.; Hong, D.; Kim, Y. J.; Jang, H.; Han, H. J.; Hwang, C. K.; Kim, D.; Kim, J.; Jung, Y. S. Efficient and sustainable water electrolysis achieved by excess electron reservoir enabling charge replenishment to catalysts. *Nat. Commun.* **2023**, *14*, 1.
(35) Freakley, S. J.; Ruiz-Esquius, J.; Morgan, D. J. The X-ray photoelectron spectra of Ir, IrO_2 and $IrCl_3$ revisited. *Surf. Interface Anal.* **2017**, *49*, 794−799.
(36) Povia, M.; Abbott, D. F.; Herranz, J.; Heinritz, A.; Lebedev, D.; Kim, B. J.; Fabbri, E.; Patru, A.; Kohlbrecher, J.; Schäublin, R.; Nachtegaal, M.; Copéret, C.; Schmidt, T. J. Operando X-ray characterization of high surface area iridium oxides to decouple their activity losses for the oxygen evolution reaction. *Energy Environ. Sci.* **2019**, *12*, 3038−3052.
(37) Zhong, H.; Zhang, Q.; Yu, J.; Zhang, X.; Wu, C.; Ma, Y.; An, H.; Wang, H.; Zhang, J.; Wang, X.; et al. Fundamental Understanding of Structural Reconstruction Behaviors in Oxygen Evolution Reaction Electrocatalysts. *Adv. Energy Mater.* **2023**, *13* (31), 2301391.
(38) Claudel, F.; Dubau, L.; Berthomé, G.; Solà-Hernández, L.; Beauger, C.; Piccolo, L.; Maillard, F. Degradation Mechanisms of Oxygen Evolution Reaction Electrocatalysts: A Combined Identical-Location Transmission Electron Microscopy and X-Ray Photoelectron Spectroscopy Study. *ACS Catal.* **2019**, *9*, 4688−4698.
(39) Blasco-Ahicart, M.; Soriano-Lopez, J.; Carbo, J. J.; Poblet, J. M.; Galan-Mascaros, J. R. Polyoxometalate electrocatalysts based on earth-abundant metals for efficient water oxidation in acidic media. *Nat. Chem.* **2018**, *10*, 24−30.
(40) Zhu, Y.; Zhou, W.; Zhong, Y.; Bu, Y.; Chen, X.; Zhong, Q.; Liu, M.; Shao, Z. A Perovskite Nanorod as Bifunctional Electrocatalyst for Overall Water Splitting. *Adv. Energy Mater.* **2017**, *7*, 1602122.
(41) Shinagawa, T.; Garcia-Esparza, A. T.; Takanabe, K. Insight on Tafel slopes from a microkinetic analysis of aqueous electrocatalysis for energy conversion. *Sci. Rep.* **2015**, *5*, 13801.
(42) Debnath, B.; Bansal, A.; Salunke, H. G.; Sadhu, A.; Bhattacharyya, S. Enhancement of Magnetization through Interface Exchange Interactions of Confined NiO Nanoparticles within the Mesopores of $CoFe_2O_4$. *J. Phys. Chem. C* **2016**, *120* (10), 5523−5533.
(43) Juodkazyte, J.; Sebeka, B.; Valsiunas, I.; Juodkazis, K. Iridium Anodic Oxidation to Ir(III) and Ir(IV) Hydrous Oxides. *Electroanalysis* **2005**, *17*, 947−952.
(44) McCrory, C. C. L.; Jung, S.; Peters, J. C.; Jaramillo, T. F. Benchmarking Heterogeneous Electrocatalysts for the Oxygen Evolution Reaction. *J. Am. Chem. Soc.* **2013**, *135*, 16977−16987.
(45) Slater, J. C. Atomic Radii in Crystals. *J. Chem. Phys.* **1964**, *41*, 3199−3204.
(46) Green, C. L.; Kucernak, A. Determination of the Platinum and Ruthenium Surface Areas in Platinum−Ruthenium Electrocatalysts by Underpotential Deposition of Copper. 2. Effect of Surface Composition on Activity. *J. Phys. Chem. B* **2002**, *106* (44), 11446−11456.
(47) Shan, J.; Guo, C.; Zhu, Y.; Chen, S.; Song, L.; Jaroniec, M.; Zheng, Y.; Qiao, S. Z. Charge-Redistribution-Enhanced Nanocrystalline Ru@IrOx Electrocatalysts for Oxygen Evolution in Acidic Media. *Chem* **2019**, *5*, 445−459.

Downloaded from pubs.acs.org/acsodf/article-pdf/11/44/69026/6903792/acsomega.6c08923.pdf by UNIVERSIDADE DO PORTO 01100 user on 25 November 2026

https://doi.org/10.1021/acsomega.6c08923
ACS Omega 2026, 11, 69026−69037